

# Effects of Externally-Through-Internally-Mixed Soot Inclusions Within Clouds and Precipitation on Global Climate

Mark Z. Jacobson

Department of Civil and Environmental Engineering, Stanford University, Stanford, California 94305-4020, USA; Email: [jacobson@stanford.edu](mailto:jacobson@stanford.edu); Tel: (650) 723-6836

*In press, J. Phys. Chem. A,*

*Submitted Nov. 4, 2005, Revised Jan. 23, 2006, Accepted Feb. 2, 2006*

This paper examines the incremental global climate response of black carbon (BC), the main component of soot, due to absorption and scattering by BC inclusions within cloud and precipitation particles. Modeled soot is emitted as an externally-mixed aerosol particle. It evolves to an internal mixture through condensation, hydration, dissolution, dissociation, crystallization, aqueous chemistry, coagulation, and cloud processing. Size-resolved cloud liquid and ice particles grow by condensation onto size resolved soot and other particles. Cloud particles grow to precipitation by coagulation and the Bergeron process. Cloud and precipitation particles also undergo freezing, melting, evaporation, sublimation, and coagulation with interstitial aerosol particles. Soot, which is tracked in cloud and precipitation particles of all sizes, is removed by rainout, washout, sedimentation, and dry deposition. Two methods of treating the optics of BC in size-resolved cloud liquid, ice and graupel are compared: the core-shell approximation (CSA) and the iterative dynamic effective medium approximation (DEMA). The 10-year global near-surface incremental temperature response due to fossil fuel (ff), biofuel (bf), and biomass burning (bb) BC within clouds with the DEMA was slightly stronger than that with the CSA, but both enhancements were  $< +0.05$  K. The ff+bf portion may be ~60% of the total, suggesting that BC inclusions within clouds may enhance the near-surface

temperature response of ff+bf soot due to all processes (estimated as  $\sim 0.27$  K), by  $<10\%$ , strengthening the possible climate impact of BC. BC cloud absorption was also found to increase water vapor, decrease precipitation, and decrease cloud fraction. The increase in water vapor at the expense of precipitation contributed to warming in addition to that of the cloud BC absorption itself. Aerosol-hydrometeor coagulation followed by hydrometeor evaporation may have caused almost twice the BC internal mixing as aerosol-aerosol coagulation.

## 1. Introduction

This study examines the incremental global climate response of black carbon (BC) due to its absorption and scattering as an inclusion within size-resolved liquid and ice cloud and precipitation particles. A few recent studies have examined the regional or global climate response of particles containing black carbon<sup>1-6</sup>. *Jacobson*<sup>2,3</sup> treated size resolution of aerosol particles, cloud liquid, cloud ice, and cloud graupel. A single discrete size distribution (17 size bins) of aerosol particles was emitted. Near strong sources, emitted particles were effectively externally mixed since they dominated particle number and mass of a given size, but they became more internally mixed away from sources due to condensation, dissolution, aqueous chemistry, and coagulation. Aerosol particles entered hydrometeor particles by nucleation scavenging and aerosol-hydrometeor coagulation. Composition-resolved aerosol inclusions were tracked within hydrometeor particles of all sizes, but absorption and scattering by BC as an inclusion within hydrometeor particles were not treated.

The remaining studies treated BC as a bulk parameter but with a single lognormal or modified gamma size distribution with assumed shape for radiative calculations. In *Wang*<sup>4</sup>, BC was treated as externally mixed only. In *Roberts and Jones*<sup>5</sup> and *Chung and Seinfeld*<sup>6</sup>, bulk BC was emitted as hydrophobic. A fraction was converted to hydrophilic

BC assuming a fixed timescale. Hydrophilic BC was removed by precipitation according to an empirical parameterization. BC inclusions within cloud drops were not treated.

Another set of studies has examined the climate response of fields of fixed aerosol optical depth with different single-scattering albedos<sup>7-10</sup>. Additional studies have looked at the direct and indirect radiative forcing change due to soot<sup>11</sup>. These studies also did not treat BC inclusions in cloud clouds or precipitation.

Black carbon affects clouds in at least three ways. When it is coated with hydrophilic material, BC may serve as a cloud condensation nucleus (CCN) or ice deposition nucleus (IDN). When it is uncoated or coated with hydrophobic material (e.g., lubricating oil), it does not serve so well as a nucleus<sup>12-15</sup>. Second, interstitial BC (BC between hydrometeor particles) may absorb and scatter radiation, affecting the temperature within and the radiation passing through clouds<sup>7,16-18</sup>. Third, BC inclusions within cloud drops, ice crystals, and graupel may affect the albedo and temperatures of clouds<sup>19-28</sup>.

To date, two studies have examined the idealized effect on atmospheric stability and temperatures of reducing the single-scattering albedo of clouds from 1.0 to 0.99, in one- and three-dimensional models, respectively<sup>26,27</sup>. However, no study to date has modeled the three-dimensional evolution of BC from emission to inclusion within hydrometeor particles together with the optical properties of BC inclusions within the hydrometeor particles and the resulting climate response.

Here 10-year time-dependent climate-response simulations of fossil-fuel soot (black carbon, organic matter, and sulfate) are reported where fossil-fuel soot is emitted into a discrete externally-mixed aerosol size distribution and evolves into a separate, discrete internally-mixed size distribution. Both the externally- and internally-mixed aerosol distributions further evolve into separate liquid, ice, and graupel hydrometeor size distributions that contain all the aerosol components they evolve from. Aerosol particles also enter hydrometeor particles by impact scavenging (hydrometeor-aerosol

coagulation). Whereas *Jacobson*<sup>2,3</sup> accounted for the effect of interstitial (between size-resolved hydrometeor particles) aerosol particles containing BC on radiative transfer and temperatures and treated inclusions within hydrometeor particles, the studies did not account for the effect of absorption and scattering by the hydrometeor inclusions. Here, this effect is treated.

Below, the model used for this study is described, numerical simulations of the climate response of fossil-fuel black soot are discussed, and results are analyzed.

## **2. Description of the Model**

The model used and modified for this study was GATOR-GCMOM, a parallelized and one-way-nested global-through-urban scale Gas, Aerosol, Transport, Radiation, General Circulation, Mesoscale, and Ocean Model<sup>1,29-33</sup>. In this section the model, prior to modification, is described.

### *2.A. Atmospheric Dynamical and Transport Processes*

The model solved the hydrostatic momentum equation and the thermodynamic energy equation with a potential-entropy, mass, and kinetic-energy-conserving scheme<sup>34</sup>. It used spherical and sigma-pressure coordinates in the horizontal and vertical, respectively. Transport of gases (including water vapor), and aerosol particle number concentration and aerosol component mole concentration within each size bin of each size distribution was solved with the scheme of *Walcek and Aleksic*<sup>35</sup> using modeled online winds and vertical diffusion coefficients.

### *2.B. Gas processes*

Gas processes included emission, photochemistry, advection, turbulence, cloud convection of gases, nucleation, washout, dry deposition, and condensation onto and dissolution into aerosols, clouds, and precipitation. Gases affected solar and thermal-IR

radiation, aerosol formation and growth, and cloud evolution, all of which fed back to meteorology. Gas photochemistry was solved with SMVGear II<sup>36</sup>. The chemical mechanism for this study included 126 gases and 283 reactions relevant to urban, free tropospheric, and stratospheric chemistry.

### *2.C. Aerosol Processes*

Aerosol processes were treated among two aerosol size distributions, each with 14 size bins and multiple components per size bin, and three hydrometeor size distributions, each with 30 bins, with each bin containing all the chemical components present in both aerosol size distributions plus either liquid, ice, or graupel. Parameters treated prognostically in each size bin of each aerosol distribution included particle number concentration and individual component mole concentration. Single-particle volume was calculated assuming particles contained a solution and nonsolution component. The setup of the aerosol size distributions and equations affecting them are given elsewhere<sup>37</sup>.

Table 1 lists the species present in each size bin of each aerosol and hydrometeor distribution. The first aerosol size distribution was that for “emitted fossil-fuel soot” (EFFS). The distribution really consisted of emitted soot plus chemicals that grew onto soot by condensation, hydration, dissolution, dissociation, and crystallization. Although growth occurred onto this distribution, it was still considered “externally mixed” for three reasons: (a) particles from all other sources were emitted into a separate distribution (“internally-mixed” or MX), (b) coagulation of EFFS with the MX distribution resulted in material moving to the MX distribution, so constituents from the MX distribution did not enter the EFFS distribution, and (b) near emission sources, emission dominated growth onto EFFS particles, so EFFS was dominated by emitted soot near sources and by soot plus a coating (due to growth) far from the sources, which should happen physically.

The material emitted into the EFFS distribution included fossil-fuel black carbon (BC), primary organic matter (POM), and S(VI) compounds ( $\text{H}_2\text{SO}_4(\text{aq})$ ,  $\text{HSO}_4^-$ , and

SO<sub>4</sub><sup>2-</sup>). Particulate matter emitted into the MX distribution included chemicals associated with biofuel combustion, biomass burning, sea spray emission, and soildust emission (Section 2.G.). Material that could condense/evaporate (in a nonequilibrium calculation) upon the EFFS distribution (and simultaneously onto the MX distribution) included sulfuric acid gas and organic gases. Each time interval following gas chemistry integration, low-vapor-pressure organic gases from the chemistry mechanism (e.g., nitrocresol, nitrophenol, isoprene nitrate, etc.) were sequestered into a single condensable surrogate organic gas. Condensation equations were subsequently solved with the mass-conserving, noniterative, positive-definite, unconditionally-stable method<sup>37</sup> between the gas phase and all size bins of both aerosol size distributions simultaneously. The particle component produced in each bin was a single surrogate species, secondary organic matter (SOM), which was treated separately from emitted primary organic matter (POM). The advantage of this method was that it allowed for a physical calculation of gas-particle transfer of organic gases as a function of particle size and vapor pressure. As computer time becomes less limited and explicit organic chemistry becomes more accurate, this generalized method easily expands to explicit gases rather than to a surrogate secondary organic, treated here.

Following condensation, nonequilibrium dissolutional growth of gas phase nitric acid and hydrochloric acid were calculated between the gas phase and each size bin of the EFFS and MX distributions. Ammonia and pH were then equilibrated simultaneously between the gas and solution phases of all particle sizes. Finally, internal aerosol composition (accounting for dissociation and crystallization), final pH, and aerosol liquid water content were determined within each size bin in an equilibrium calculation. All calculations accounted for nonideality of solution through the use of solute activity coefficients. The processes just described were solved with PNG-EQUISOLV II<sup>38</sup>, where PNG is Predictor of Nonequilibrium Growth and EQUISOLV II<sup>39</sup> is a chemical equilibrium code that calculates aerosol liquid water content, pH, and ion concentrations

following nonequilibrium growth. The solver treats nonequilibrium gas-particle growth at long time step for multiple dissociating acids and a base.

Homogenous nucleation of sulfuric acid-water-ammonium produced new particles in the MX distribution, Ternary nucleation rates were calculated from *Napari et al.*<sup>40</sup>. At low ammonia mixing ratios, binary sulfuric acid-water nucleation rates were calculated from *Vehkamaki et al.*<sup>41</sup>. Homogeneous nucleation was solved simultaneously with condensation of sulfuric acid onto the EFFS and MX distributions in order to allow competition of sulfuric acid vapor between nucleation and condensation, as described elsewhere<sup>37</sup>.

Self-coagulation of either EFFS or MX particles moved the particles and their components to larger sizes in their respective distributions. Heterocoagulation of EFFS with MX particles moved EFFS particles and their components to the MX distribution. The scheme used to solve coagulation among multiple size distributions was volume- and volume-concentration conserving, noniterative, positive-definite, and unconditionally stable<sup>37</sup>. Aerosol particles were removed by dry deposition, sedimentation, rainout, and washout. Interaction of aerosol particles with clouds is discussed next.

#### *2.D. Gas-Aerosol-Cloud-Turbulence Interactions*

Cloud thermodynamics and microphysics were solved substantially as in *Jacobson*<sup>42</sup>. Briefly, each cloud-process time interval, equilibrium (non-time-dependent) cumulus and stratus parameterizations were used to solve for subgrid bulk cloud/precipitation liquid water and ice in each grid cell of a column. The cloud and precipitation water was then forcibly evaporated and regrown, in a nonequilibrium calculation, onto size-resolved aerosol particles. Additional microphysical calculations followed. Cloud properties at the middle of the time-interval were fed back to radiative calculations. At the end of the time interval, clouds were forcibly evaporated and remaining hydrometeor-particle cores converted back to aerosol particles so that a new equilibrium/nonequilibrium calculation

could be performed for the next time interval. Thus, subgrid clouds were not transported horizontally, but water vapor was.

The stratus and cumulus parameterizations used accounted for subgrid scale cloud formation and cloud fraction. The stratus cloud scheme was from *Mellor and Yamada*<sup>43</sup> and was coupled with the calculation of turbulence (order 2.5). The stratus scheme modeled cloud fraction and cloud water content in each layer given turbulence terms and vertical gradients in potential temperature and moisture. Turbulence parameters affected clouds, momentum, energy, and tracers, particularly in the boundary layer, which was resolved. Cumulus clouds and precipitation were modeled with a modified Arakawa-Schubert algorithm<sup>44</sup>. In each column, nearly 500 subgrid cumulus clouds could form (and 1-10 typically formed), each defined by a unique cloud base and top (when 23 layers existed below the tropopause, 22 bases and 22 tops are possible). For each subgrid cloud, water and energy transport were solved with a mass-flux convection scheme; gas and size-resolved aerosol component transport were solved with a positive-definite, stable convective plume transport scheme. Because aerosol particles were transported vertically with cloud water in all cases, aerosol activation was consistent with that in a rising plume. For each subgrid cloud, the model also generated adjustments to large-scale potential temperature, momentum, and water vapor.

Following equilibrium cloud and precipitation formation, the bulk water predicted in each layer from all resulting subgrid clouds was forcibly evaporated/sublimated and regrown (simultaneously for liquid and ice) onto the two size-resolved aerosol distributions transported to the layer. For the calculation, the total number concentration of particles in each size bin of each aerosol distribution was divided into ice deposition nuclei (IDN), cloud condensation nuclei (CCN), and neither, as described elsewhere<sup>42</sup>. The fractions were based on current aerosol composition in the bin and the probability of a given component allowing activation. Nonequilibrium condensation and deposition equations were then solved simultaneously among the gas phase and all CCN and IDN in

all size bins of both distributions. Thus, when supercooled clouds formed, deposition competed with condensation for the limited amount of vapor available, allowing precipitation particles to form by the Bergeron process. Precipitation also formed by hydrometeor-hydrometeor coagulation, discussed shortly.

The growth calculation resulted in liquid and ice hydrometeor particles and unactivated aerosol particles. The liquid and ice hydrometeor particles were each given their own hydrometeor size distribution with 30 size bins, and the unactivated aerosol particles remained in the aerosol distribution. Each size bin of the new liquid hydrometeor distribution was described by a particle number concentration and contained condensed liquid water plus all the chemical components of the underlying aerosol particles that the liquid water condensed upon, including liquid water hydrated to ions in the aerosol particles. The new ice distribution was analogous. A third discretized hydrometeor distribution, graupel, was also tracked. The graupel distribution formed upon heterocoagulation of liquid water with ice hydrometeor distributions, contact freezing of aerosol particles with the liquid distribution, heterogeneous-homogeneous freezing of the liquid distribution, and evaporative freezing of the liquid distribution. Graupel also contained aerosol inclusions.

Following creation of the liquid and ice distributions, time-dependent, size-resolved processes treated included (a) liquid-liquid, liquid-ice, liquid-graupel, ice-ice, ice-graupel, and graupel-graupel hydrometeor coagulation, (b) coagulation of interstitial aerosol particles with hydrometeor liquid, ice, and graupel, (c) liquid drop breakup, (d) hydrometeor sedimentation, (e) evaporative cooling during drop settling below cloud base, (f) evaporative freezing (freezing of a liquid drop as it begins to evaporate below cloud base), (g) heterogeneous-homogeneous freezing, (h) contact freezing, (i) melting, (j) sublimation, (k) release of aerosol cores upon evaporation/sublimation, (l) irreversible aqueous chemistry, (m) gas uptake and washout, (n) lightning generation from size-resolved coagulation bounceoff among ice and graupel hydrometeors, and (o)

sedimentation. Sedimentation of size-resolved liquid, ice, and graupel and their components not only removed hydrometeor particles from the current layer but also added them to the current layer when sedimentation from above occurred. The coagulation kernel for all cloud interactions and aerosol-cloud interactions included a coalescence efficiency and collision kernels for Brownian motion, Brownian diffusion enhancement, turbulent inertial motion, turbulent shear, settling, thermophoresis, diffusio-phoresis, and electric charge.

During the microphysical calculations just described, changes in energy due to condensation, evaporation, deposition, sublimation, freezing, and melting were included as diabatic heating terms in the thermodynamic energy equation, which was solved with the other dynamical equation. Energy was conserved exactly due to cloud formation and decay. Similarly, total water (water vapor, size-resolved aerosol water, size-resolved cloud water, soil water, and ocean water) was conserved exactly.

Size-resolved clouds and precipitation removed aerosol particles of different size by two mechanisms: nucleation scavenging and aerosol-hydrometeor coagulation. Both processes were size-resolved with respect to both aerosol particles and hydrometeor particles.

## *2.E. Radiative Processes*

Radiation processes included UV, visible, solar-IR, and thermal-IR interactions with gases, size/composition-resolved aerosols, and size/composition-resolved hydrometeor particles. Radiative transfer was solved with a two-stream method<sup>45</sup>. Calculations were performed for >600 wavelengths/probability intervals and affected photolysis and heating. Gas absorption coefficients in the solar-IR and thermal-IR were calculated for H<sub>2</sub>O, CO<sub>2</sub>, CH<sub>4</sub>, CO, O<sub>3</sub>, O<sub>2</sub>, N<sub>2</sub>O, CH<sub>3</sub>Cl, CFC<sub>3</sub>, CF<sub>2</sub>Cl<sub>2</sub>, and CCl<sub>4</sub> with a multiple-gas absorption method<sup>46</sup> that uses HITRAN data. Aerosol-particle optical properties were calculated assuming that black carbon (BC) (if present in a size bin) comprised a

particle's core and all other material coated the core. Shell real and imaginary refractive indices for a given particle size and wavelength were obtained by calculating the solution-phase refractive index from partial molar refraction theory, calculating refractive indices of non-solution, non-BC species, and volume averaging solution and nonsolution refractive indices. Aerosol core and shell refractive indices were used in a core-shell Mie-theory calculation<sup>47</sup>. *Schnaiter et al.*<sup>48</sup> found that this approximation matches measurements well for thick coatings. The surface albedos of snow, sea ice, and water (ocean and lake) were wavelength-dependent and predicted by (rather than specified in) the model<sup>3</sup>. Column calculations treated shading by structures (e.g., buildings) and topography. Section 3 describes cloud optics.

## *2.F. Subgrid Surfaces and Oceans*

The model treated ground temperatures over subgrid surfaces (up to 12 soil classes and roads, roofs, and water in each grid cell). It also treated vegetation over soil, snow over bare soil, snow over vegetation over soil, sea-ice over water, and snow over sea-ice over water<sup>31</sup>. For all surfaces except sea ice and water, surface and subsurface temperatures and liquid water were found with a time-dependent 10-layer module. Ocean mixed-layer velocities, energy transport, and mass transport were calculated with a gridded 2-D potential-entrophy, kinetic energy, and mass-conserving shallow-water equation module, forced by wind stress<sup>49</sup>, based on a shallow-water scheme<sup>34</sup>. The actual depth at each location was a prognostic variable, but because the module conserved volume exactly, the average mixing depth over the global ocean was constant (80 m). For lake water, a fixed 80 m mixing depth was assumed. Water (ocean and lake) temperatures were also affected by sensible, latent, and radiative fluxes. For this work, nine additional layers were treated below each ocean mixed-layer grid cell to treat energy diffusion from the mixed layer to the deep ocean and ocean chemistry. Dissolution of gases to the ocean and ocean chemistry were calculated with OPD-EQUISOLV O<sup>50</sup>, where OPD solves nonequilibrium

transport between the ocean and atmosphere and EQUISOLV O solves chemical equilibrium in the ocean. Both schemes are mass conserving and unconditionally stable.

## 2.G. Emission

Fossil-fuel soot was emitted into the EFFS aerosol distribution and was assumed to consist of BC, POM, and S(VI). The primary organic matter:primary organic carbon (POM:POC) ratio of emitted organics was set to 1.6, the ambient urban value given by *Turpin and Lim*<sup>51</sup>. The POM:POC ratio for ambient aerosols may vary from 1.2 to 3.2, with an average for nonurban aerosols of 2.1<sup>51</sup>, but since the ratio needed here is for emission only, the urban value is most relevant.

Table 2 shows the global emission rate of fossil-fuel BC and POC assumed here. Most of the baseline gridded (1°x1° resolution) inventory for submicron BC originated from *Bond et al.*<sup>52</sup>. From that inventory, U.S. emissions of BC and POC were replaced by that from the U.S. National Emission Inventory for 1999, version 2<sup>53</sup> and those for shipping were replaced as described in the footnote to Figure 2. BC emission from aircraft were not included although they will be included in future work. Such emission are approximately 0.005 Tg-C/yr<sup>56</sup>, which is approximately 0.05% of total global BC emission (Table 2).

Biofuel and biomass-burning BC and POC were also obtained from *Bond et al.*<sup>52</sup>, but without replacement. These emissions were sent into the internally-mixed (MX) rather than the EFFS aerosol distribution. The yearly BC and POC biomass-burning gridded inventories of *Bond et al.*<sup>52</sup> were distributed monthly by scaling them to a monthly BC inventory, as described elsewhere<sup>33</sup>. Emission rates of other species emitted in biomass burning and biofuel burning aside from BC and POC were calculated as follows. Emission rates of particle components K<sup>+</sup>, Na<sup>+</sup>, Ca<sup>2+</sup>, Mg<sup>2+</sup>, NH<sub>4</sub><sup>+</sup>, Cl<sup>-</sup>, SO<sub>4</sub><sup>2-</sup>, and NO<sub>3</sub><sup>-</sup>, and gases CO<sub>2</sub>, CO, CH<sub>4</sub>, N<sub>2</sub>O, NO<sub>x</sub>, SO<sub>2</sub>, ethene, propene, ethane, and propane, were obtained by multiplying the monthly gridded BC emission rates by the ratio of the

mean biofuel or biomass-burning emission factor for each gas or particle component to that of BC<sup>57</sup>. The ions K<sup>+</sup>, Ca<sup>2+</sup>, and Mg<sup>2+</sup> were not carried in the simulations, but their mole-equivalent emissions were added to those of Na<sup>+</sup>. Coarse BC and POC emissions for all sources were estimated as 25% and 45% those of fine BC and POC emissions, respectively<sup>3</sup>.

Other particles directly emitted included sea spray (treated as H<sub>2</sub>O(aq), Na<sup>+</sup>, Cl<sup>-</sup>, and POM, with mole-equivalent emissions of K<sup>+</sup>, Ca<sup>2+</sup>, and Mg<sup>2+</sup> added as Na<sup>+</sup>), soil dust (treated as generic), and pollen/spores. Particle mass emissions into each aerosol size distribution (EFFS or MX) were placed into model size bins after being discretized from multimodal lognormal distributions. Gases emitted included biogenic isoprene, monoterpenes, other volatile organics, nitric oxide, and nitrous oxide, lightning NO<sub>x</sub>, ocean DMS, volcanic SO<sub>2</sub>, anthropogenic CO<sub>2</sub>, N<sub>2</sub>O, H<sub>2</sub>, H<sub>2</sub>O, CO, CH<sub>4</sub>, paraffins, olefins, formaldehyde, higher aldehydes, toluene, xylene, NO, NO<sub>2</sub>, HONO, NH<sub>3</sub>, SO<sub>2</sub>, SO<sub>3</sub>, H<sub>2</sub>SO<sub>4</sub>.

### **3. Treatment of Cloud Optics**

This section describes the numerical treatment of cloud optics used for this study. In each model grid cell, the model provided the number concentration of each size bin of each of the five size distributions (two aerosol distributions and three hydrometeor distributions) shown in Table 1 and the mole concentration of each chemical component (shown in Table 1) in each size bin of each distribution. When no cloud was present in the grid cell, only the aerosol distributions and gases affected optics. The radiative transfer code (Section 2.E) was applied in a column calculation at each of > 600 wavelengths and probability intervals through the column each radiation time interval (4 hours). The code required the wavelength-dependent optical depth, single-scattering albedo, and asymmetry parameter from each grid cell in the column, accounting for gas, aerosol, and cloud optics.

Optical properties at a given wavelength of hydrometeor particles of a given size were calculated with the Mie code described in Section 2.E. Liquid drops were assumed to be spherical. Ice crystals and graupel were assumed to be nonspherical. Their nonsphericity was modeled as a collection of spheres of the same total volume to area ratio and total volume as the nonspherical particle<sup>58</sup>. Thus, for example, each single ice crystal was modeled as multiple individual spherical ice crystals. The use of several smaller spheres, compared with the use of a single sphere, has been shown to enhance scattering closer to the correct solution for randomly-oriented circular cylinders of any dimension<sup>58</sup>.

At least three practical methods exist of treating optics of inclusions within hydrometeor particles in a three-dimension model. With all methods, single-particle scattering, absorption, and forward scattering efficiencies are determined with a Mie code.

With the first method, the refractive indices for use in the Mie code are derived from an effective-medium approximation, such as the volume-average refractive index mixing rule, the volume average dielectric constant mixing rule<sup>59</sup>, the Maxwell-Garnett mixing rule<sup>60</sup>, or the Bruggeman mixing rule<sup>61</sup>. These mixing rules give an average complex refractive index of a particle as a whole given the volume fractions and complex refractive indices of both the medium and an absorbing substance within it. When two materials of similar optical properties are mixed, all four of the effective medium approximations give similar results. However, when a strongly absorbing material mixes with a nonabsorbing material, the Bruggeman and Maxwell-Garnett mixing rules give results more comparable with experimental data<sup>62</sup>. A disadvantage of all four effective medium approximations is that they give the same result at a given wavelength for a given volume fraction of an absorbing substance, regardless of the size distribution of the substance within the medium. A second disadvantage is that they do not treat light interactions as a function of inclusion size.

With the second method, the refractive indices for use in the Mie code are derived from a dynamic effective medium approximation that accounts for polydispersion of spherical absorbing inclusions within the medium<sup>21,63</sup>. This technique gives different efficiencies for the same volume fraction but different size distributions of absorbing material, as occurs in reality. It also accounts for light interactions that are a function of size of the inclusions. With this method, the effective dielectric constant  $\epsilon_{\text{eff}}$  (and thus the effective refractive index) of a mixture containing water and size-distributed absorbing inclusions within it is calculated from<sup>21</sup>

$$(1 - V) \frac{\epsilon_w - \epsilon_c}{\epsilon_w + 2} + V \frac{\epsilon_c - \epsilon_c}{\epsilon_c + 2} + \frac{2}{45} \frac{\epsilon_c - \epsilon_c}{\epsilon_c} \left( \frac{\epsilon_c - \epsilon_c}{\epsilon_c} \right)^2 \left[ 1 + \frac{5}{2} \frac{\epsilon_c - \epsilon_c}{\epsilon_c + 3} + \frac{18}{(\epsilon_c + 2)^2} \int_0^\infty r^5 n(r) dr \right] = 0 \quad (1)$$

where  $V$  is the volume fraction of absorbing inclusions in a mixture of water and inclusions,  $\omega$  is the circular frequency of light ( $2\pi c / \lambda$ ) ( $\text{s}^{-1}$ ),  $c$  is the speed of light ( $\text{cm s}^{-1}$ ),  $\lambda$  is wavelength ( $\text{cm}$ ),  $\epsilon_w$  is the dielectric constant of water,  $\epsilon_c$  is the dielectric constant of the inclusions,  $r$  is the radius of an inclusion, and  $n(r)$  is the number concentration of inclusions per unit radius interval ( $\text{inclusions/cm}^3\text{-cm}$ ). This equation includes a corrected squared term inadvertently missing in Equation 4 of the original paper<sup>21</sup>. Equation 1 assumes that the inclusions are sufficiently small that  $|m_c x| \ll 1$ , where  $m_c = \sqrt{\epsilon_c}$  is the complex refractive index of the inclusion and  $x = 2r/\lambda$  is the size parameter. The equation represents a useful approximation beyond that range as well<sup>21,64</sup>. Chylek<sup>64</sup> discusses the extent of the limits in some detail. A complex dielectric constant is related to real and imaginary refractive indices ( $n, k$ ) and real and imaginary dielectric constants ( $\epsilon_r, \epsilon_i$ ) by  $m_c^2 = (n - ik)^2 = \epsilon_r - i\epsilon_i$ , leading to  $\epsilon_r = n^2 - k^2$ ,  $\epsilon_i = 2nk$ ,  $n = \sqrt{(\sqrt{\epsilon_r^2 + \epsilon_i^2} + \epsilon_r)/2}$  and  $k = \sqrt{(\sqrt{\epsilon_r^2 + \epsilon_i^2} - \epsilon_r)/2}$ . In the limit of infinitely small inclusions, the last term in Equation 1 disappears and the result simplifies to Bruggeman

mixing rule. Equation 1 is solved iteratively, but it requires only 3-5 iterations for convergence in nearly all cases.

With the third method, all absorbing material in a particle is aggregated into a single core inclusion placed at the center of the drop, and a Mie code for stratified spheres is used to solve for efficiencies assuming a shell of water surrounds the core (e.g., Section 2.E).

Figure 1 compares absorption efficiencies as a function of wavelength resulting from the three methods discussed. The Bruggeman mixing rule is used to represent the first method. The example assumes a single liquid water drop of diameter 12.599  $\mu\text{m}$  and a volume fraction of black carbon of  $V=10^{-6}$  (Fig. 1a) or  $V=10^{-5}$  (Fig. 1b).

Figure 1 shows that the dynamic effective medium approximation (DEMA) always gives greater absorption efficiencies than does the Bruggeman mixing rule, which the DEMA simplifies to in the limit of infinitely small inclusions. Logically, then, the figure also shows that, with the DEMA method, larger monodisperse inclusions (0.2  $\mu\text{m}$  diameter) result in greater absorption than do smaller monodisperse inclusions (0.1  $\mu\text{m}$  diameter) when the volume fraction of inclusions is the same in both cases. The figure also shows that, at longer visible wavelengths, the core/shell method results in more absorption than do the other methods, but the reverse is true at shorter visible wavelengths. Further, as BC volume fraction increases, the core/shell method produces less absorption at all wavelengths relative to the other methods, since the absorption efficiency of many small inclusions overpowers the absorption efficiency of a single large inclusion more and more at increasing volume fraction. This last conclusion was found earlier by *Chylek et al.*<sup>21</sup>, who showed that, at 0.5- $\mu\text{m}$  wavelength, the core-shell treatment gave similar specific absorption coefficients to those of the dynamic effective medium approximation when 0.1- $\mu\text{m}$  inclusions were assumed, so long as the volume fraction of absorbing material was less than about  $3 \times 10^{-6}$ .

In *Jacobson*<sup>3</sup>, the globally-averaged concentration of BC in rain and snow was modeled to be about 22 ng/g and the maximum instantaneous value anywhere was about 640 ng/g, corresponding to volume fractions of BC of about  $3.3 \times 10^{-8}$  and  $9.6 \times 10^{-7}$ , respectively. As such, for precipitation, the results in Fig. 1a would be more applicable. In clouds, though, the volume fraction of BC has a greater range, sometimes increasing to  $10^{-4}$ . Thus, it is necessary to account for a variable BC fraction in clouds and precipitation, which is done here, as described next.

For this study, 3-D climate responses of the effect of scattering and absorption by BC inclusions within hydrometeor particles are compared when the dynamic effective medium and the core-shell approximations are made. When the DEMA is used, it is ideal to track a size distribution of BC within hydrometeor particles of each size rather than to use a monodisperse distribution. However, here, a monodisperse distribution of BC within hydrometeor particles is used for the following reasons.

Black carbon is comprised of aggregates of individual spherules that each range from 5-50 nm in diameter with an average 25-35 nm diameter<sup>65,66</sup>. The BC aggregates are often coated with lubricating oil and some sulfate, giving a soot particle. One study found that about 68% of soot mass was BC<sup>67</sup>. The mean diameter of the emitted soot aggregates is usually between 50-100 nm, although the possible range is 30-1000 nm. During combustion, small 2-30-nm particles are also emitted, but these generally consist of sulfate and lubricating oil, with little or no black carbon<sup>68</sup>. In the atmosphere, soot particles grow by condensation/dissolution of gases and coagulation. Condensation changes the size of the soot particle as a whole but not the size of the black carbon inclusion within the soot particle (except to the extent that compaction makes soot particle more spherical<sup>48</sup>). Similarly, coagulation changes the size of the whole particle but it changes the size of BC in the particle to a lesser extent and not at all if the coagulation is between a soot particle and a non-soot particle. Because the sizes of BC inclusions within aerosol particles change much less than do the sizes of the particles as a whole

during aging, it should not be unreasonable to assume that, when soot particles enter hydrometeor particles, the sizes of the individual BC inclusions in the aerosol particles and now, in the hydrometeor particles, are only a little larger than the emitted size of the BC inclusions.

Thus, for application of the DEMA in this study, it was assumed that the size distribution of BC inclusions within hydrometeor particles was monodisperse with a mean diameter of 0.1  $\mu\text{m}$ , a little larger than their emitted size (0.05 to 0.1  $\mu\text{m}$  with a peak near 0.07  $\mu\text{m}$ ). The number concentration of 0.1- $\mu\text{m}$  inclusions within an individual hydrometeor particle was determined as the mole concentration of BC among all hydrometeor particles of a given size in a given distribution (which was a prognostic variable) multiplied by the molecular weight of carbon, divided by the mass density of BC (assumed to be 1.5  $\text{g}/\text{cm}^3$ ), by the number concentration of hydrometeor particles in the size bin (also a prognostic variable), and by the spherical volume of a single 0.1- $\mu\text{m}$  particle.

The use of a monodisperse distribution within hydrometeor particles was also necessary in the present simulation to limit computer time and memory. The model can track the size distribution of each chemical component within each hydrometeor particle size bin. Such components enter hydrometeor particles during nucleation scavenging and aerosol-hydrometeor coagulation. However, tracking such components requires an order of magnitude increase in memory and computer time. Instead, the mole concentration of each component within each hydrometeor size bin was summed over all aerosol size bins within the hydrometeor bin and, for DEMA optical calculations, the size distribution of the BC was assumed to be monodisperse.

In contrast with the DEMA, which allows multiple inclusions of realistic size, the CSA allows a single BC inclusion within each hydrometeor particle. The volume of the inclusion was determined here as the mole concentration of BC multiplied by its molecular weight and divided by the mass density of black carbon and by the number

concentration of hydrometeor particles in the size bin. The CSA is physically realistic only when the hydrometeor particle shrinks due to evaporation since, as hydrometeor particles evaporate, their involatile inclusions must physically become more concentrated and eventually coalesce into one inclusion. Although the mole concentrations of components aside from BC were tracked in hydrometeor particles, their effect on hydrometeor optics was not treated to isolate the effects of BC.

#### **4. Description of Simulations**

Three ten-year simulations were run. The simulations each required about six months of computer time on three 2.6 GHz Intel Xeon processors. All simulations were identical, except for one difference. In all three cases, BC inclusions were treated within hydrometeor particles, but in the baseline simulation, the optics of hydrometeor particles, determined with a Mie code, were assumed not to be affected by the BC inclusions (“Baseline case”). In the first sensitivity test, the Mie calculation was performed assuming each hydrometeor particle contained a single BC core, if it existed, surrounded by a water shell (“CSA case”). In the second sensitivity test, the Mie calculation was performed assuming each hydrometeor particle contained multiple monodisperse BC inclusions surrounded by water, and the refractive indices of the particle were found from the dynamic effective medium approximation (“DEMA case”). The DEMA case took approximately 10% more computer time than did the CSA case due to the additional iterations required for all wavelengths and hydrometeor sizes and distributions in the DEMA case.

In all cases, meteorology was initialized with National Center for Environmental Prediction (NCEP) reanalysis fields for August 1, 1999, at 12 GMT<sup>69</sup>. The model dynamics time step was 300 s. Aerosol and gas fields in all domains were initialized as in Ref. 3. No data assimilation, nudging, or model spinup was performed during any simulation.

Emissions of all components from all sources (Section 2.G) were the same in all simulations. Thus, for example, soot emission included soot from fossil-fuel, biofuel, and biomass burning in all cases. In each of the two sensitivity tests, the BC treated for hydrometeor optics included BC from all three sources. Thus, the results here isolated the effect of BC from all sources rather than just those from fossil-fuel sources. The results, though, can be scaled by the relative emission to get a rough estimate of the contribution of each major source of BC to enhanced cloud absorption.

## 5. Results

Figure 2 shows the modeled 10-year averaged baseline BC concentration (a) near the surface in the EFFS distribution, (b) zonally averaged in the EFFS distribution, (c) near the surface in the MX distribution, and (d) zonally-averaged in the MX distribution. About 42% of BC (that from fossil-fuel sources) was emitted in the EFFS distribution (Table 2). The rest, from biofuel and biomass burning sources, was emitted into the MX distribution. BC from the EFFS distribution also entered the MX distribution by aerosol-aerosol coagulation and by aerosol-hydrometeor coagulation followed by hydrometeor evaporation. As hydrometeor particles evaporate, their involatile inclusions must physically become more concentrated and eventually coalesce into one inclusion. In the model, individual aerosol inclusions were assumed to coalesce in this way, and upon complete evaporation in the air, the inclusion was released back to its actual size in the MX aerosol distribution. Those hydrometeor particles that reached the ground as precipitation released their aerosol inclusions to the snow, sea ice, water, or other surfaces. In the case of snow and sea ice, the BC inclusions affected albedo<sup>3</sup>.

Of the total near-surface BC mass in Figs. 2a and c, about 4.5% resided in the EFFS distribution, indicating that, in steady state, about 90% of emitted EFFS ( $100\% \times (42\% - 4.5\%) / 42\%$ ) became internally mixed due to aerosol-aerosol coagulation and aerosol-hydrometeor coagulation. Most of the internal mixing was due to aerosol-

hydrometeor coagulation followed by evaporation since, as shown in Fig. 1a of *Jacobson*<sup>30</sup>, an earlier version of the model used here determined that aerosol-aerosol coagulation caused only 35% of BC mass to internally mix within 5 days. The difference in the present simulation (90%-35%=65%) was most likely due to cloud processing, which was not treated in the previous study. Thus, aerosol-hydrometeor coagulation followed by hydrometeor evaporation may have caused almost twice as much internal mixing as did aerosol-aerosol coagulation.

Figures 2a and 2c show that concentrations of BC were greatest over land. Figures 2b and 2d show that BC penetrated globally in both the horizontal and vertical. *Pueschel et al.*<sup>70</sup> measured the concentration of BC at 20 km from about 70° S to 60° N North to be between <0.1 and 2.6 ng/m<sup>3</sup>. *Blake and Kato*<sup>71</sup> similarly measured BC at 18-21 km in the Northern Hemisphere to be between 0.01 and 2.6 ng/m<sup>3</sup>. Although some of this may be due to aircraft BC, *Petzold et al.*<sup>56</sup> estimated that <0.1 ng/m<sup>3</sup> of BC in the upper troposphere was due to aircraft, thus less in the stratosphere. The sum of Figs. 2b and 2d here indicate that the zonally-averaged BC concentration from the model at 20 km was approximately 0.7 ng/m<sup>3</sup>, indicating little numerical diffusion and a mean value well within the measured range of BC at 20 km. *Pueschel et al.*<sup>70</sup> measured 0.1-2.5 ng/m<sup>3</sup> BC at 9-11 km. *Blake and Kato*<sup>71</sup> measured 0.1-3.4 ng/m<sup>3</sup> BC at 9-11 km. The mean modeled value at 10 km was approximately 2.5 ng/m<sup>3</sup>, at the upper end of the measured ranges.

Figure 3 shows the modeled 10-year averaged baseline column total aerosol mass and number (1 nm-diameter), respectively, summed over the EFFS and MX distributions. Whereas total aerosol mass was dominated by soil dust from the Sahara, sea spray from the oceans, and anthropogenic sources, aerosol number was dominated primarily by anthropogenic sources (including fossil-fuel, biomass and biofuel burning), which were mostly on land. The highest number concentrations of particles were modeled to be in China, India, and Europe, where significant emission of nanoparticles and homogeneous nucleation of sulfuric acid were modeled to occur.

Figure 4 shows the vertical profile of the ten-year and globally-averaged differences between the DEMA and baseline cases and the CSA and baseline cases, respectively, for several parameters. The first parameter (Fig.4a) is temperature. The figure shows that the DEMA and CSA resulted in  $< +0.05$  K increase in near-surface air temperature. Fossil-fuel plus biofuel (ff+bf) BC is approximately 60% of total BC, suggesting that the incremental near-surface climate response due to ff+bf BC absorption in clouds was  $<10\%$  of that due to other processes (about  $0.27$  K)<sup>3</sup>.

The DEMA approximation resulted in a larger increase in free-tropospheric temperatures (up to  $+0.2$  K) than did the CSA case (up to  $+0.05$  K). In the stratosphere, the DEMA case resulted in a smaller change in temperature than did the CSA case, but since air density in the stratosphere is so low, the changes in temperature there suggest very small changes in energy in both cases.

The stronger tropospheric warming in the DEMA case appears to have been due in part because cloud absorption, integrated over all UV, visible, and solar-IR wavelengths, was greater in the DEMA case than in the CSA case. At 550 nm, though, clouds absorbed more in the CSA case than in the DEMA case (Fig. 4b), a result expected from Fig. 1. Fig. 1 shows that clouds absorb more at short solar wavelengths but less at longer solar wavelengths when the DEMA is used than when the CSA is used. As the volume fraction of BC in a cloud drop increases, the more clouds absorb at longer and shorter wavelengths with the DEMA than with the CSA. Fig. 1, in fact, suggests that at very low volume fraction of BC, the integrated absorption due the CSA exceeds that of the DEMA. As the BC volume fraction increases, the integrated absorption due to the DEMA begins to dominate, even though absorption with the CSA remains stronger at midvisible wavelengths. The stronger integrated absorption due to the DEMA simultaneous with the stronger 550-nm absorption due to the CSA can be illustrated with the following calculation. For a  $10.085\text{-}\mu\text{m}$  diameter cloud drop with a black carbon volume fraction of  $8 \times 10^{-6}$ , the single-scattering albedo at 550 nm with the CSA

(0.99379) is less than that with the DEMA (0.99396), indicating stronger relative absorption to scattering by the CSA at 550 nm, but the single-scattering albedo, integrated over all solar wavelengths (by weighting each wavelength interval by the solar flux in the interval) with the DEMA (0.984772) is less than that with the CSA (0.984816), indicating stronger total relative absorption by the DEMA.

Figures 4d and 4e show that the net downward solar irradiance decreased and the net downward thermal-IR irradiance increased more with the DEMA than with the CSA. Since the solar irradiance is integrated over all solar wavelengths, this result is consistent with the stronger spectrally-integrated absorption by clouds with the DEMA compared with the CSA. However, part of the stronger reduction in solar and increase in thermal-IR due to the DEMA was due to an additional feedback, the enhancement of water vapor by the DEMA more than with the CSA (Fig. 4f and Table 3). Water vapor is both a greenhouse gas and solar absorber. The absorption spectrum of water vapor used in the present study is given in *Jacobson*<sup>46</sup>. Water vapor increased more in the DEMA case relative to the CSA case because the DEMA case decreased precipitation (Table 3), cloud liquid water (Table 3 and Fig. 4g), and cloud ice (Table 3 and Fig. 4h), and much of this water vaporized (Table 3 and Fig. 4f). The water vapor acted as a greenhouse gas and solar absorber to warm the air further, which in turn, led to more evaporation of cloud water and less precipitation. Since precipitated water does not warm the air, the replacement of precipitation by water vapor in the DEMA case caused a net warming of the troposphere relative to the CSA. The effect warming due to the additional water vapor contributed, along with the warming due enhanced cloud absorption integrated over all wavelengths, to a greater increase in temperatures and decrease in surface solar irradiance in the DEMA case relative to the CSA case.

The greater reduction in downward solar irradiance in the DEMA case resulted in a greater increase in the solar heating rate in that case (Fig. 4i) relative to the CSA case. Conversely, the greater increase in the net downward thermal-IR resulted in a greater

decrease in the thermal-IR heating rate in the DEMA versus CSA case (Fig. 4j). However, the loss of thermal-IR was smaller than the gain in solar heating, resulting in an increase in temperature in the DEMA relative to the CSA case (Fig. 4a).

The greater reduction in downward solar irradiance in the DEMA case resulted in a greater increase in the solar heating rate in that case (Fig. 4i) relative to the CSA case. Conversely, the greater increase in the net downward thermal-IR resulted in a greater decrease in the thermal-IR heating rate in the DEMA versus CSA case (Fig. 4j). However, the loss of thermal-IR was smaller than the gain in solar heating, resulting in an increase in temperature in the DEMA relative to the CSA case (Fig. 4a).

An additional factor that led to the stronger absorption by CSA at 550 nm was the fact that less BC entered cloud water in the DEMA case than in the CSA case. This is evidenced by the lower precipitation content of BC in rainwater in the DEMA case (Table 1) and follows logically from the fact that less cloud water was present in the DEMA case than in the CSA case (Table 1), so aerosol-hydrometeor coagulation rates were lower in the DEMA case.

Although DEMA resulted in lower 550-nm cloud absorption optical depths, it resulted in greater 550-nm cloud scattering optical depth than did CSA (Fig. 4c) and 550-nm total optical depth (Table 3). This was expected since absorption reduces scattering. In addition, DEMA increased the number of small drops and ice crystals (Table 3), which have a greater reflectivity than a smaller number of large drops or ice crystals. DEMA resulted in a greater number of small drops because it had smaller overall liquid water and ice contents (Table 3 and Figs. 4i,j) than did CSA, and lower water contents result, at first, in smaller particles, which slow hydrometeor-hydrometeor coagulation rates, thereby increasing the number of hydrometeor particles. The slower coagulation rates also reduced precipitation for the DEMA relative to the CSA (Table 3).

Figure 5 shows spatial difference plots for some parameters in the two cases. The DEMA case increased near-surface temperatures primarily in the Northern Hemisphere

and decreased them primarily in the Southern Hemisphere (possibly due to local feedbacks of clouds to large-scale meteorology), resulting in a small net warming (Fig. 5a). The CSA case resulted in a similar small net near-surface warming (Table 3), but less regional variation in temperature. Fig. 5b shows that most of the warming in the vertical profile of temperature in the DEMA case from Fig. 4a was due to warming in northern latitudes. Similarly, the water vapor increase in the DEMA case occurred primarily in northern latitudes (Fig. 5c). The 550-nm cloud optical depth in the DEMA case increased primarily over land and decreased over the ocean relative to the base case (Fig. 5d), giving a globally-averaged net increase (Table 3). The net decrease in cloud optical depth in the CSA case resulted from a strong decrease over land in Northern Africa that was not offset by increases elsewhere. The greater 550-nm cloud absorption optical depth in the CSA case relative to the DEMA case occurred almost everywhere (Fig. 5e), indicating that the main reason for the stronger 550-nm absorption in the CSA case was the stronger absorption efficiency of BC at 550 nm relative to other wavelengths, as illustrated in Figure 1. Although the average global reductions in cloud fraction in the DEMA and CSA cases were small ( $<0.1\%$ , Table 3), Fig. 5f indicates that maximum reductions or increases in cloud fraction ranged from  $\pm 5\%$ .

## **6. Conclusions**

The GATOR-GCMOM model was modified to treat absorption and scattering of aerosol inclusions within individual hydrometeor particles. The modified model was used to examine the incremental global climate response of black carbon (BC), the main component of soot, due to BC inclusions within hydrometeor particles. Modeled soot was emitted as an external mixture. It evolved to an internal mixture through several microphysical and chemical processes and through cloud processing. Size-resolved cloud liquid and ice particles formed by condensation of water vapor onto size resolved soot and other particles. Cloud particles grew to precipitation particles coagulation and the

Bergeron process. Cloud and precipitation particles also underwent freezing, melting, evaporation, sublimation, and coagulation with interstitial aerosol particles. Soot, which was tracked in cloud and precipitation particles of all sizes, was removed by rainout, washout, sedimentation, and dry deposition.

Two methods of treating the optics of BC in size-resolved cloud liquid, ice and graupel were compared: the core-shell approximation (CSA) and the dynamic effective medium approximation (DEMA). The 10-year global near-surface incremental temperature response due to fossil fuel (ff), biofuel (bf), and biomass burning (bb) BC within clouds with the DEMA was slightly stronger than that with the CSA, but both enhancements were  $< +0.05$  K. Since the ff+bf portion may be 60% of the total, BC absorption within hydrometeor particles may enhance the near-surface temperature response of ff+bf soot, estimated as  $\sim 0.27$  K, by  $< 10\%$ . This increase strengthens BC's position as possibly the second most important component of global warming after carbon dioxide.

In both the CSA and DEMA cases, absorption was found to decrease precipitation and increase water vapor. The increase in water vapor at the expense of precipitation contributed to warming beyond that caused by BC absorption within clouds itself. Aerosol-hydrometeor coagulation followed by hydrometeor evaporation was also modeled to cause almost twice as much internal mixing of BC as aerosol-aerosol coagulation.

### **List of Acronyms**

BC – Black Carbon

CCN – Cloud Condensation Nucleus

CSA – Core-Shell Approximation

DEMA – Dynamic Effective Medium Approximation

EFFS – Emitted Fossil-Fuel Soot

GATOR-GCMOM – Gas, Aerosol, TranspOrt, Radiation, General Circulation,  
Mesoscale, and Ocean Model

IDN – Ice Deposition Nucleus

MX – Internally-Mixed

OPD – Ocean Predictor of Dissolution

POC – Primary Organic Carbon

POM – Primary Organic Matter

PNG – Predictor of Nonequilibrium Growth

SMVGEAR II – Sparse-Matrix Vectorized Gear Code II

SOM – Secondary Organic Matter

### **Acknowledgement**

This work was supported by the National Aeronautics and Space Administration.

## References and Notes

1. Jacobson, M.Z. *Atmos. Environ.*, **1997b**, *31A*, 587-608.
2. Jacobson, M.Z. *J. Geophys. Res.*, **2002a**, *107*, (D19), 4410, doi:10.1029/2001JD001376.
3. Jacobson, M.Z. *J. Geophys. Res.*, *109*, **2004b**, doi:10.1029/2004JD004945.
4. Wang, C. *J. Geophys. Res.*, **2004**, *109*, D03106, doi:10.1029/2003JD004084.
5. Roberts, D.L.; Jones, A. *J. Geophys. Res.*, **2004**, *109*, D16202, doi:10.1029/2004JD004676.
6. Chung, S.H.; Seinfeld, J.H. *J. Geophys. Res.*, **2005**, *110*, D11102, doi:10.1029/2004JD005441.
7. Hansen, J.; Sato, M.; Ruedy R. *J. Geophys. Res.*, **1997**, *102*, 6831-6864.
8. Menon, S.; Hansen, J.; Nazarenko, Y.L. *Science*, **2002**, *297*, 2250-2253,
9. Hansen, J.; Nazarenko, L. *Proc. Natl. Acad. Sci.*, **2003**, doi/10.1073/pnas.2237157100.
10. Cook, J.; Highwood, E.J. *Q.J.R. Meteorol. Soc.*, **2004** *130*, 175-191.
11. Penner, J.E.; Zhang, S.Y.; Chuang, C.C. *J. Geophys. Res.*, **2003**, *108* (D21), 4657, doi:10.1029/2003JD003409.
12. Lammel, G.; Novakov, T. *Atmos. Environ.*, **1995**, *29*, 813-823.
13. Weingartner, E.; Burtscher, H.; Baltensperger, U. *Atmos. Environ.*, **1997**, *31*, 2311-2327.
14. Kristjansson, J. E. *J. Geophys. Res.*, **2002**, *107*, (D15), 10.1029/2001JD000887.
15. Ishizaka, Y.; Adhikari, M. Composition of cloud condensation nuclei, *J. Geophys. Res.*, **2003**, *108* (D4), 4138, doi:10.1029/2002JD002085.
16. Ackerman, A.S.; Toon, O.B.; Stevens, D.E.; Heymsfield, A.J.; Ramanathan, V.; Welton, E.J. *Science*, **2000**, *288*, 1042-1047.
17. Johnson, B.T., Shine, K.P.; Forster, P.M. *Q.J.R. Meteorol. Soc.*, **2004**, *130*, 1407-1422.
18. Koren, I.; Kaufman, Y.J.; Remer, L.A.; Martins, J.V. *Science*, **2004**, *303*, 342-345.

19. Danielson, R. E.; Moore, D. R.; van de Hulst, H.C. *J. Atmos. Sci.*, **1969**, *26*, 1078-1087.
20. Grassl, H. *Contrib. Atmos. Phys.*, **1975**, *48*, 199-210.
21. Chylek, P.; Ramaswamy, V.; Cheng, R.J. *J. Atmos. Sci.* **1984**, *41*, 3076-3084.
22. Chylek, P.; Hallett, J. *Q. J. R. Meteorol. Soc.*, **1992**, *118*, 167-172.
23. Chylek, P.; Lesins, G.; Videen, G.; Wong, J. G. D.; Pinnick, R. G.; Ngo, D.; Klett, J. *D. J. Geophys. Res.*, **1996**, *101*, 23,365-23,372.
24. Twohy, C.H.; Clarke, A.D.; Warren, S.G.; Radke, L.F.; Charlson, R.J. *J. Geophys. Res.*, **1989**, *94*, 8623-8631.
25. Erlick, C.; Russell, L.M.; Ramaswamy, V. *J. Geophys. Res.*, **2001**, *106*, 1249-1269.
26. Erlick, C.; Ramaswamy, V. *J. Geophys. Res.*, **2003**, *108* (D16), 4522, doi:10.1029/2002JD002966.
27. Erlick, C.; Ramaswamy, V.; Russell, L.M., *J. Geophys. Res.*, in press, **2006**.
28. Conant, W.C.; Nenes, A.; Seinfeld, J.H. *J. Geophys. Res.*, **2002**, *107* (D21), 4604, doi:10.1029/2002JD002094.
29. Jacobson, M.Z. *Atmos. Environ.*, **1997a**, *31A*, 131-144.
30. Jacobson, M.Z. *Nature*, **2001a**, *409*, 695-697.
31. Jacobson, M.Z. *J. Geophys. Res.*, **2001b**, *106*, 5385-5402.
32. Jacobson, M.Z. *J. Geophys. Res.*, **2001c**, *106*, 5403-5420.
33. Jacobson, M.Z. *J. Clim.*, **2004a**, *17* (15), 2909-2926.
34. Arakawa, A.; Lamb, V.R. *Mon. Wea. Rev.*, **1981**, *109*, 18-36.
35. Walcek, C.J.; Aleksic, N.M. *Atmos. Environ.*, **1998**, *32*, 3863-3880.
36. Jacobson, M.Z. *Atmos. Environ.*, **1998**, *32*, 791-796.
37. Jacobson, M.Z. *J. Geophys. Res.*, **2002b**, *107* (D19), 4366, doi:10.1029/2001JD002044.
38. Jacobson, M.Z. *Aerosol Sci. Technol.*, **2005a**, *39*, 92-103.
39. Jacobson, M.Z. *Atmos. Environ.*, **1999**, *33*, 3635-3649.

40. Napari I.; Noppel M.; Vehkamaki H.; Kulmala M. *J. Geophys. Res.*, **2002**, *107* (D19), 4381, doi:10.1029/2002JD002132.
41. Vehkamaki, H.; Kulmala, M.; Napari, I.; Lehtinen, K.E.J.; Timmreck, C.; Noppel, M.; Laaksonen, A. *J. Geophys. Res.*, **2002**, *107* (D22), 4622, doi:10.1029/2002JD002184.
42. Jacobson, M.Z. *J. Geophys. Res.*, **2003**, *108* (D8), 4245, doi:10.1029/2002JD002691.
43. Mellor, G. L.; Yamada, T. *Revs. of Geophys. and Space Phys.*, **1982**, *20*, 851-875.
44. Ding, P.; Randall, D. A. *J. Geophys. Res.*, 1998, *103*, 11,341-11,353.
45. Toon, O.B.; McKay, C.P.; Ackerman, T. P.; Santhanam, K. *J. Geophys. Res.*, **1989**, *94*, 16,287-16,301.
46. Jacobson, M.Z. *J. Atmos. Sci.*, **2005b**, *62*, 506-517.
47. Toon, O.B.; Ackerman, T.P. *Appl. Opt.*, **1981**, *20*, 3657-3660.
48. Schnaiter, M; Linke, C.; Mohler, O.; Naumann, K.-H.; Saathoff, H.; Wagner, R.; Schurath, U.; Wehner, B. *J. Geophys. Res.*, **2005**, *110*, D19204, doi:10.1029/2005JD006046.
49. Ketefian G., Jacobson, M.Z. *Mon. Weath. Rev.*, in review, 2005a.
50. Jacobson, M.Z. *J. Geophys. Res.*, **2005c**, *110*, D07302, doi:10.1029/2004JD005220.
51. Turpin, B.J.; Lim, H.-J. *Aerosol Sci. Technol.*, **2001**, *35*, 602-610.
52. Bond, T.C.; Streets, D.G.; Yarber, K.F.; Nelson, S.M.; Woo, J.-H.; Klimont, Z. *J. Geophys. Res.*, **2004**, *109*, D14203, doi: 10.1029/2003JD003697.
53. United States Environmental Protection Agency (USEPA). Clearinghouse for Inventories and Emission Factors, <http://www.epa.gov/ttn/chief/>, 2005.
54. Corbett, J.J.; Fischbeck, P.S.; Pandis, S.N. *J. Geophys. Res.*, **1999**, *104*, 3457-3470.
55. Corbett, J.J.; Koehler, H.W. *J. Geophys. Res.*, **2003**, *108* (D20), 4650, doi:10.1029/2003JD003751.
56. Petzold, A.; Doppelheuer, A.; Brock, C.A.; Schroder, F. *J. Geophys. Res.*, **1999**, *104*, 22,171-22,181.

57. Andreae, M.O; Merlet, P. *Global Biogeochemical Cycles*, **2001**, *15*, 955-966.
58. Grenfell, T.C.; Warren, S.G. *J. Geophys. Res.*, **1999**, *104*, 31,697-31,709.
59. Bohren, C.F.; Huffman, D.R. *Absorption and scattering of light by small particles*; John Wiley and Sons, New York, 530 pp., 1983.
60. Maxwell Garnett, J.C. *Philos. Trans. R. Soc.*, **1904**, *A203*, 385-420.
61. Bruggeman, D.A.G. *Ann. Phys. Leipzig*, **1935**, *24*, 636-679.
62. Chylek, P.; Srivastava, V.; Pinnick, R. G.; Wang, R.T. *Appl. Optics*, **1988**, *27*, 2396-2404.
63. Stroud, D.; Pan, F.P. *Phys. Rev.*, **1978**, *B17*, 1602-1610.
64. Chylek, P. Effective medium approximations for heterogeneous particles, in Mishchenko, M.I.; Hovenier, J.W.; Travis, L.D., Eds., *Light Scattering by nonspherical particles: Theory, Measurements, and Applications*, Academic Press, San Diego, pp. 273-308., 1999.
65. Wentzel, M.; Gorzawski, H.; Naumann, K.-H.; Saathoff, H.; Weinbruch, S. *Journal of Aerosol Science*, **2003**, *34*, 1347-1370.
66. Park, K., Kittelson, D.B.; McMurry, P.H. *Aerosol Sci. Technol.*, **2004**, *38*, 881-889.
67. Norbeck, J.M.; Durbin, T.D.; Truex, T.J. Final Report for CRC Project No. E-24-2, 1998.
68. Sakurai, H.; Tobias, H.J.; Park, K.; Zarling, D.; Docherty, K.; Kittelson, D.B.; McMurry, P.H.; Ziemann, P.J. *Atmospheric Environment*, **2003**, *37*, 1199-1210.
69. National Centers for Environmental Prediction (NCEP), 2.5 degree global final analyses, distributed by the Data Support Section, National Center for Atmospheric Research, 2003.
70. Pueschel, R.F.; Boering, K.A.; Verma, S.; Howard, S.D.; Ferry, G.V.; Goodman, J.; Allen, D.A.; Hamill, P. *J. Geophys. Res.*, **1997**, *102*, 13113-13118.
71. Blake, D.F.; Kato, K. *J. Geophys. Res.*, **1995**, *100*, 7195-7202.

## Figure Captions

**Figure 1.** (a) Single particle absorption efficiency, as a function of wavelength, of a 12.599- $\mu\text{m}$  diameter cloud drop containing a black carbon (BC) volume fraction of  $V=10^{-6}$ , where the absorption efficiency is calculated from a Mie code assuming either (i) the refractive index of the entire drop is determined from the dynamic effective medium approximation with 2 monodisperse 0.1- $\mu\text{m}$  diameter BC inclusions (DEMA1), (ii) the refractive index of the entire drop is determined from the dynamic effective medium approximation with 0.25 monodisperse 0.2- $\mu\text{m}$  diameter BC inclusions (DEMA2), (iii) the refractive index of the entire drop is determined from the Bruggeman mixing rule (Brug), and (iv) the entire particle consists of a single BC core of 0.12599  $\mu\text{m}$  in diameter surrounded by a water shell (Core/shell). (b) Same as (a), but for a BC volume fraction of  $V=10^{-5}$ . In this case, the number of monodisperse cores in the DEMA1 and DEMA2 cases were 20 and 2.5, respectively, and the single core in the CSA case was 0.2714  $\mu\text{m}$  in diameter. Fractional numbers of monodisperse cores represent an average number of BC inclusions over multiple cloud drops or ice crystals of a given size.

**Figure 2.** Modeled 10-year averaged baseline BC concentration (from all sources) (a) near the surface in the EFFS distribution, (b) zonally averaged in the EFFS distribution, (c) near the surface in the MX distribution, and (d) zonally-averaged in the MX distribution.

**Figure 3.** Modeled 10-year averaged baseline (a) column total aerosol mass and (b) column total aerosol number ( $> 1$  nm-diameter).

**Figure 4.** Modeled differences in the 10-year- and globally- averaged vertical profiles of several parameters between the DEMA and baseline cases and the CSA and baseline cases. The bottom value in the temperature figure is ground temperature.

**Figure 5.** Modeled differences between the baseline case (1999) and the sensitivity case (no absorption/scattering by BC inclusions), averaged over 10 years, in several parameters. Figures on the left were obtained with the core-shell approximation. Those on the right, with the DEMA (assuming 0.1- $\mu\text{m}$  diameter BC inclusions).

**Table 1.** Aerosol and hydrometeor size distributions treated in the model and the chemical constituents present in each size bin of each size distribution.

Emitted Fossil-Fuel Soot (14 size bins)	Internally Mixed (14 size bins)	Cloud / Precipitation Liquid (30 size bins)	Cloud / Precipitation Ice (30 size bins)	Cloud / Precipitation Graupel (30 size bins)
BC	BC	BC	BC	BC
POM	POM	POM	POM	POM
SOM	SOM	SOM	SOM	SOM
H <sub>2</sub> O(l)-hydrated	H <sub>2</sub> O(aq)-hydrated	H <sub>2</sub> O(aq)-hydrated	H <sub>2</sub> O(aq)-hydrated	H <sub>2</sub> O(aq)-hydrated
H <sub>2</sub> SO <sub>4</sub> (aq)	H <sub>2</sub> SO <sub>4</sub> (aq)	H <sub>2</sub> SO <sub>4</sub> (aq)	H <sub>2</sub> SO <sub>4</sub> (aq)	H <sub>2</sub> SO <sub>4</sub> (aq)
HSO <sub>4</sub> <sup>-</sup>	HSO <sub>4</sub> <sup>-</sup>	HSO <sub>4</sub> <sup>-</sup>	HSO <sub>4</sub> <sup>-</sup>	HSO <sub>4</sub> <sup>-</sup>
SO <sub>4</sub> <sup>2-</sup>	SO <sub>4</sub> <sup>2-</sup>	SO <sub>4</sub> <sup>2-</sup>	SO <sub>4</sub> <sup>2-</sup>	SO <sub>4</sub> <sup>2-</sup>
NO <sub>3</sub> <sup>-</sup>	NO <sub>3</sub> <sup>-</sup>	NO <sub>3</sub> <sup>-</sup>	NO <sub>3</sub> <sup>-</sup>	NO <sub>3</sub> <sup>-</sup>
Cl <sup>-</sup>	Cl <sup>-</sup>	Cl <sup>-</sup>	Cl <sup>-</sup>	Cl <sup>-</sup>
H <sup>+</sup>	H <sup>+</sup>	H <sup>+</sup>	H <sup>+</sup>	H <sup>+</sup>
NH <sub>4</sub> <sup>+</sup>	NH <sub>4</sub> <sup>+</sup>	NH <sub>4</sub> <sup>+</sup>	NH <sub>4</sub> <sup>+</sup>	NH <sub>4</sub> <sup>+</sup>
NH <sub>4</sub> NO <sub>3</sub> (s)	Na <sup>+</sup>	Na <sup>+</sup>	Na <sup>+</sup>	Na <sup>+</sup>
	NH <sub>4</sub> NO <sub>3</sub> (s)	NH <sub>4</sub> NO <sub>3</sub> (s)	NH <sub>4</sub> NO <sub>3</sub> (s)	NH <sub>4</sub> NO <sub>3</sub> (s)
	Pollen/spores	Pollen/spores	Pollen/spores	Pollen/spores
	Soildust	Soildust	Soildust	Soildust
		H <sub>2</sub> O(aq)-condensed	H <sub>2</sub> O(s)	H <sub>2</sub> O(s)

The number concentration of particles in each size bin of each size distribution was also tracked. H<sub>2</sub>O(aq)-hydrated is liquid water hydrated to dissolved ions and undissociated molecules in solution. H<sub>2</sub>O(aq)-condensed is water that has condensed to form liquid hydrometeors. Condensed and hydrated water exist in the same particles so that, if condensed water evaporates, the core material, including its hydrated water, remains. H<sub>2</sub>O(s) is either water that froze from the liquid phase or that directly deposited from the gas phase as ice.

**Table 2.** Emission rates (Tg-C/yr) of fossil-fuel black carbon and organic carbon used.

	(a) Fossil-Fuel U.S.	(d) Fossil-Fuel Shipping	(c) All other Fossil Fuel globally	(d) Total Fossil Fuel (a+b+c)	(e) Biofuel	(f) Biomass burning	(g) Total (d+e+f)
Fine BC	0.592	0.147	2.698	3.437	1.634	3.324	8.395
Coarse BC	0.370	0.037	0.675	1.082	0.409	0.831	2.322
Fine POC	2.635	0.047	2.371	5.053	6.490	25.01	36.55
Coarse POC	3.131	0.021	1.067	4.219	2.921	11.25	18.39

Fine and coarse BC and POC fossil-fuel emissions in the U.S. were obtained from the U.S. National Emission Inventory<sup>53</sup>. Fine BC emission from shipping was estimated by dividing the gridded, monthly sulfur shipping emission rate from *Corbett et al.*<sup>54</sup>, which totaled 4.24 Tg-S/yr, by 29.5 g-S/kg-fuel [*Corbett and Koehler*<sup>55</sup>, Table 1, for 1999 data] and multiplying the result by 1.02 g-BC-C/kg-fuel for shipping<sup>52</sup>. That for POC was obtained in the same manner, but by multiplying the result by 0.33 g-POC-C/kg-fuel<sup>52</sup>. Fine BC and POC for all other fossil-fuel sources globally were obtained from *Bond et al.*<sup>54</sup> after subtracting out U.S. and ocean emissions. The totals from *Bond et al.*<sup>54</sup> before subtracting out such emissions were 3.040 Tg-BC-C/yr and 2.408 Tg-POC-C/yr. Fine biofuel and biomass-burning BC and POC emissions were obtained from *Bond et al.*<sup>54</sup>. Coarse BC and POC emissions for all sources were estimated as 25% and 45% those of fine BC and POC emissions, respectively<sup>3</sup>. The emission rate of S(VI) from fossil fuels was 1% that of BC+POM+S(VI). Fossil-fuel components were emitted into the EFFF distribution.

**Table 3.** Globally-averaged difference in several parameters resulting from the DEMA versus baseline and the CSA versus baseline simulations, respectively.

Parameter	DEMA-base	CSA-base
Near-surface air temperature (K)	+0.032	+0.024
Ground temperature (K)	+0.018	+0.034
Near-surface relative humidity (out of 1)	+0.0016	-0.0038
Vertically-integrated cloud drop number (drops/cm <sup>3</sup> )	+0.03	-0.07
Vertically-integrated ice crystal number (crystals/cm <sup>3</sup> )	+0.00007	+0.00001
550 nm cloud total optical depth	+0.04	-0.04
550 nm cloud absorption optical depth	+0.000007	+0.0002
Cloud liquid water (g/m <sup>2</sup> )	-0.02	-0.005
Cloud ice (g/m <sup>2</sup> )	-0.006	+0.01
Precipitation (mm/day)	-0.01	-0.0014
Cloud fraction	-0.001	-0.0003
Water vapor (g/m <sup>2</sup> )	+232	+34.9
Tropopause solar irradiance (W/m <sup>2</sup> )	-0.06	+0.29
Tropopause thermal IR irradiance (W/m <sup>2</sup> )	+0.05	-0.07

Figure 1.

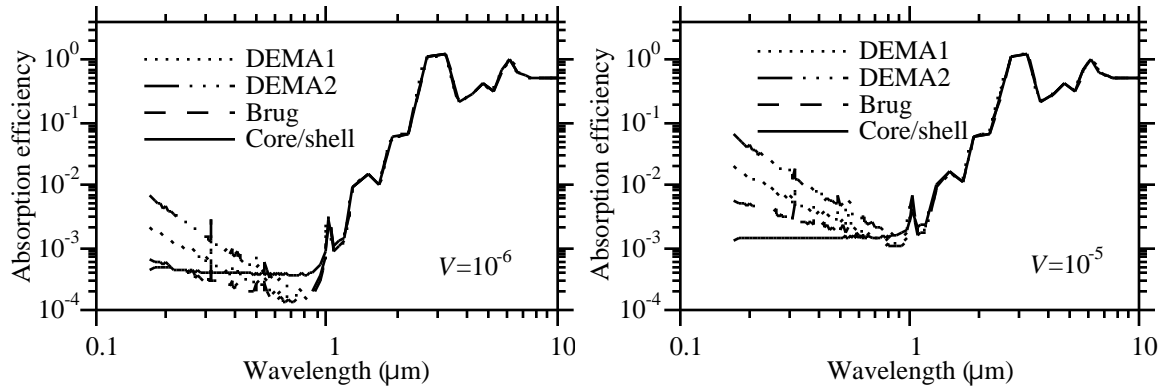
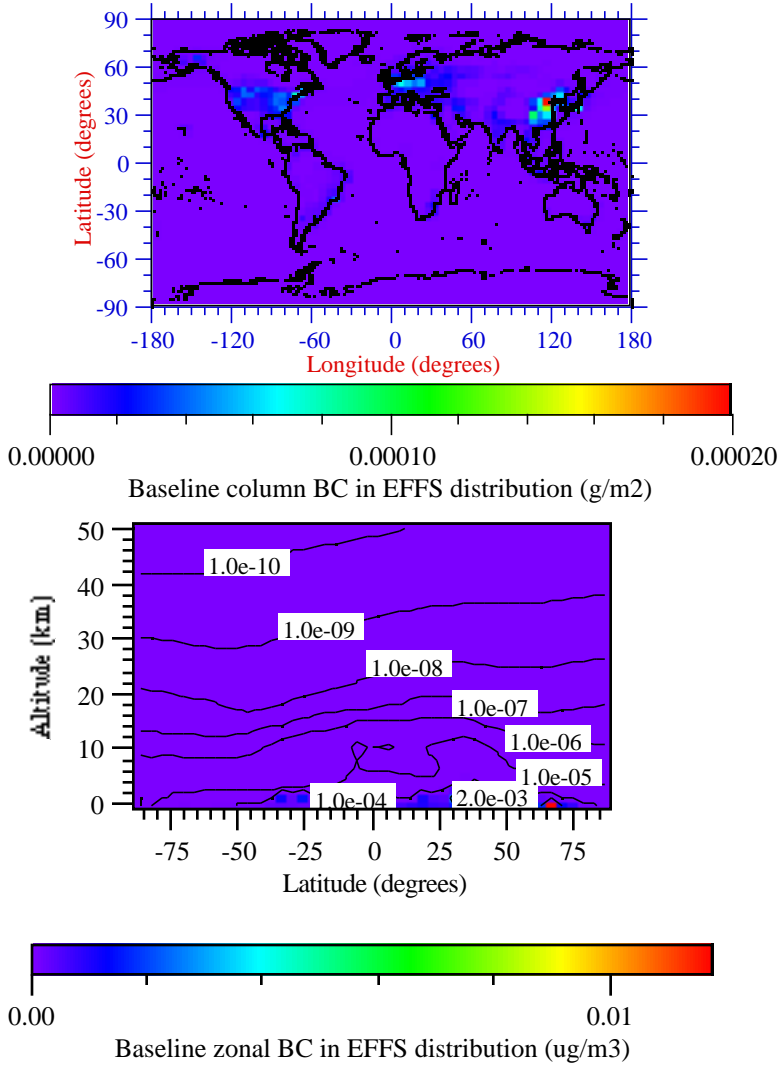
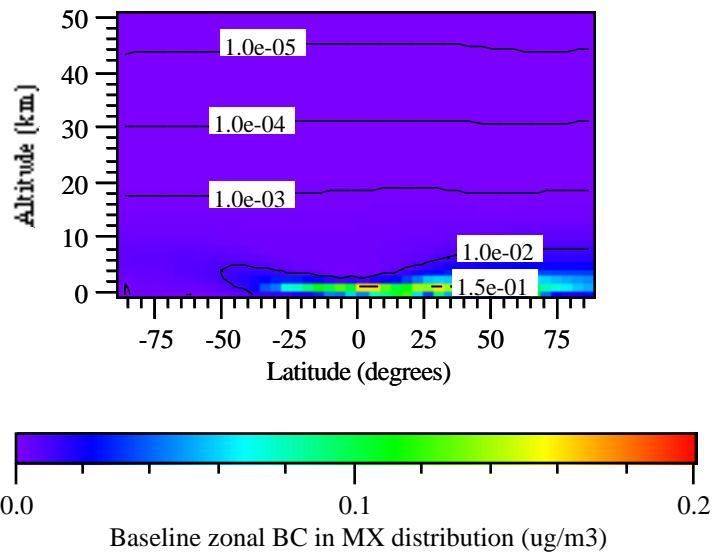
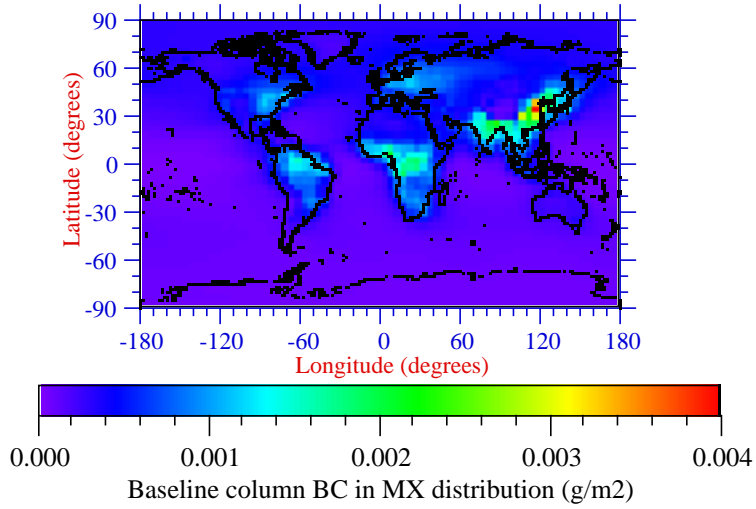
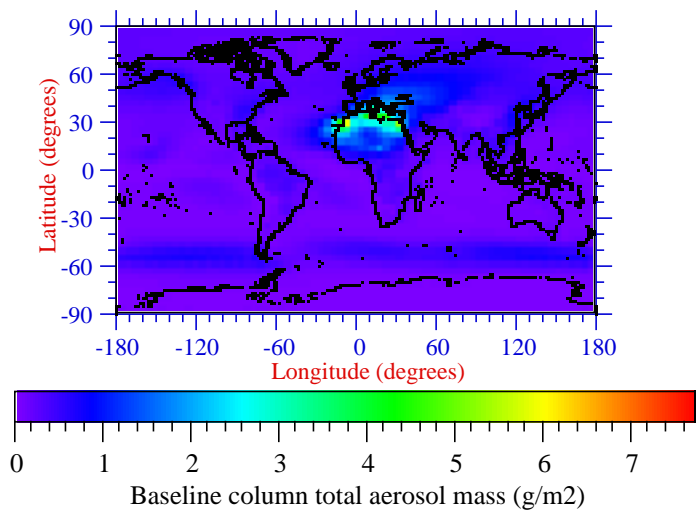


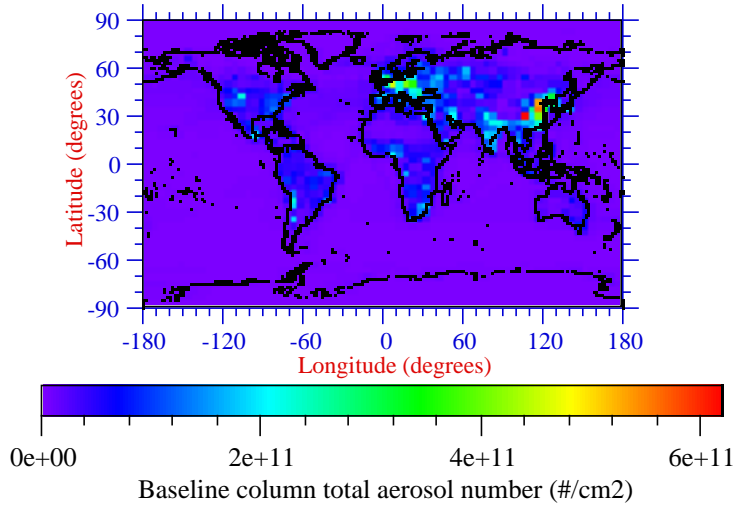
Figure 2 (a-d)



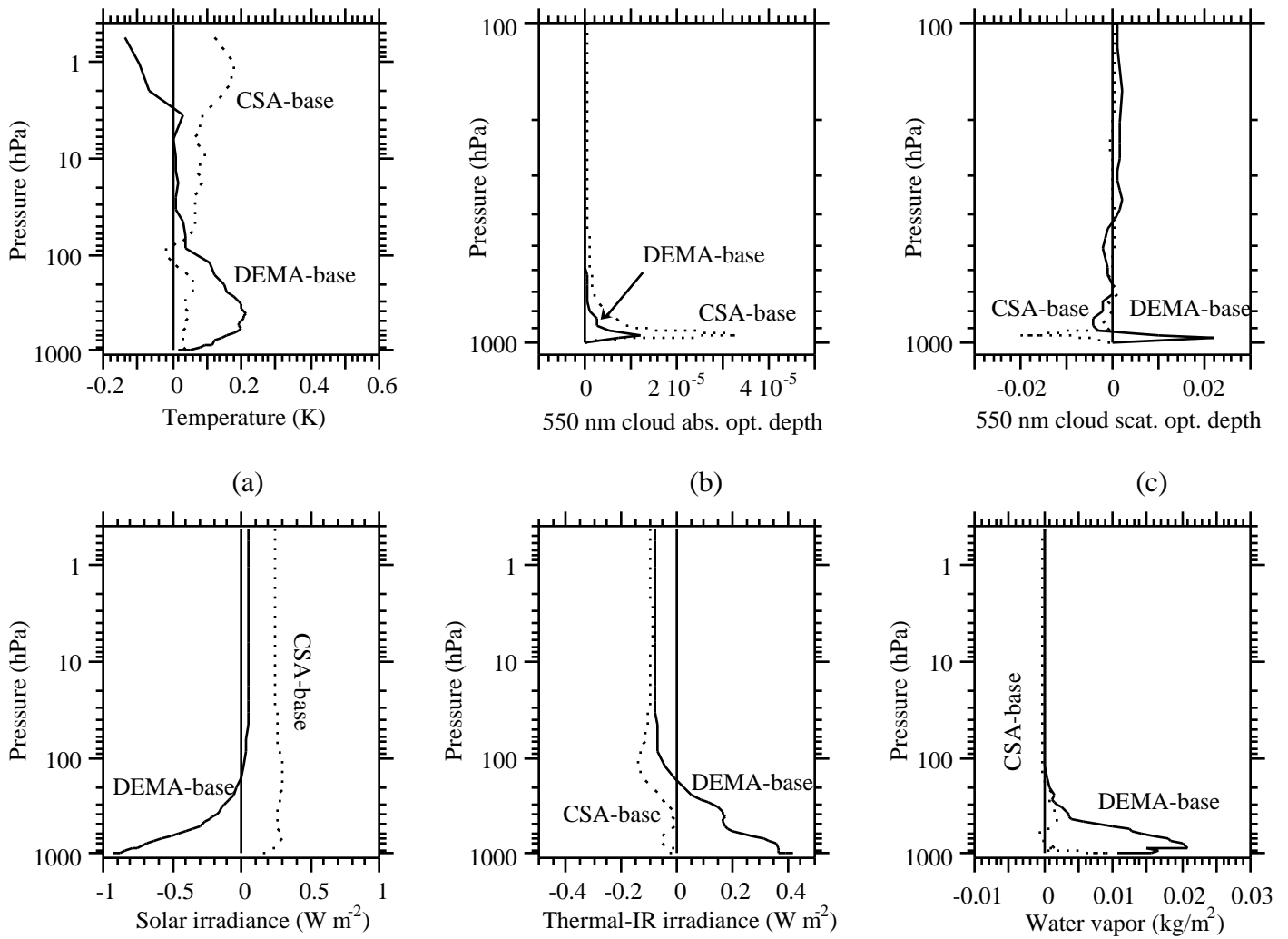


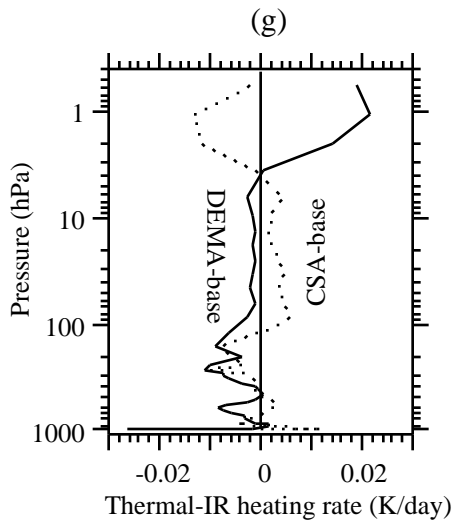
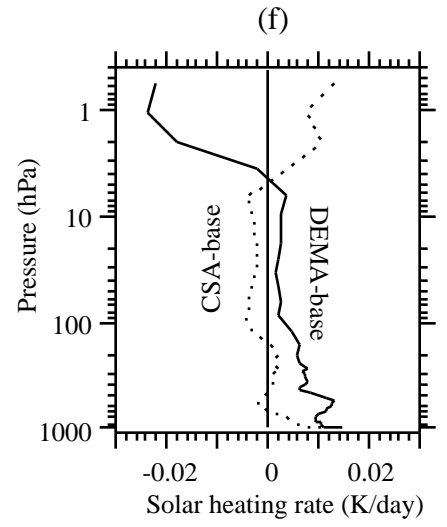
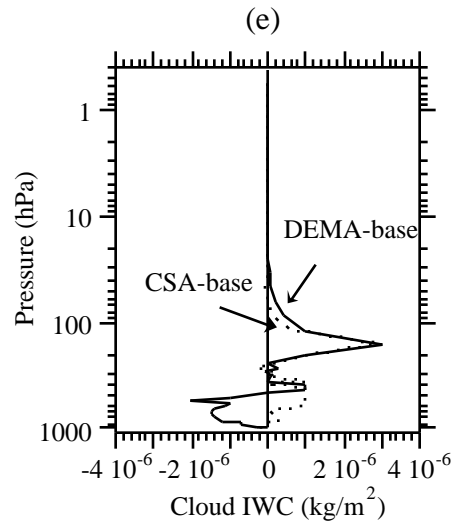
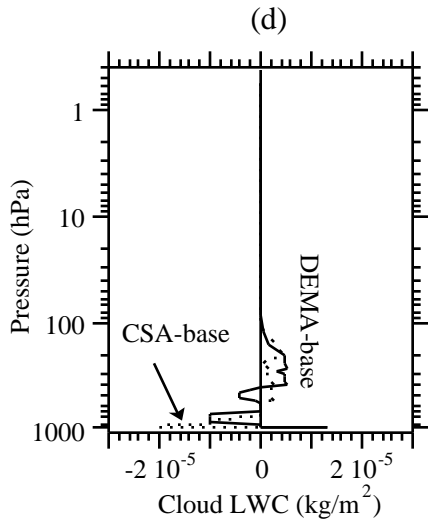
**Figure 3 (a-b)**





**Figure 4**





(j)

Figure 5 (a)

